

Micromagnetic simulation of magnetic small-angle neutron scattering from two-phase nanocomposites

Andreas Michels^{a,*}, Sergey Erokhin^b, Dmitry Berkov^b, Nataliya Gorn^b

^aLaboratory for the Physics of Advanced Materials, University of Luxembourg, 162A Avenue de la Faiencerie, L-1511 Luxembourg, Luxembourg

^bINNOVENT Technology Development, Prüßingstraße 27B, D-07745 Jena, Germany

Abstract

The recent development of a micromagnetic simulation methodology—suitable for multiphase magnetic nanocomposites—permits the computation of the magnetic microstructure and of the associated magnetic small-angle neutron scattering (SANS) cross section of these materials. In this review article we summarize results on the micromagnetic simulation of magnetic SANS from two-phase nanocomposites. The decisive advantage of this approach resides in the possibility to scrutinize the individual magnetization Fourier contributions to the total magnetic SANS cross section, rather than their sum, which is generally obtained from experiment. The procedure furnishes unique and fundamental information regarding magnetic neutron scattering from nanomagnets.

Keywords: small-angle neutron scattering, micromagnetism, nanocomposites

1. Introduction

Small-angle neutron scattering (SANS) is one of the most important techniques for microstructure determination in soft and hard condensed matter, materials science, and in physical chemistry. Since most SANS studies focus on nuclear rather than magnetic scattering, it is not surprising that the theoretical concepts behind nuclear SANS are rather well developed [1–9]. By contrast, the understanding of magnetic SANS is still at its beginning, although magnetic SANS has previously demonstrated great potential for resolving the spin structures of various magnetic materials. For instance (in the last decade), magnetic SANS has been employed for studying the microstructures of magnetic nanocomposites [10–19], amorphous alloys [20–23], and of elemental nanocrystalline bulk ferromagnets [24–35], the process of dynamic nuclear polarization [36], imaging of the flux-line lattice in superconductors [37, 38], precipitates in steels [39], nanocrystalline rare-earth metals with random paramagnetic susceptibility [40], fractal magnetic domain structures in NdFeB permanent magnets [41], spin structures of ferrofluids, nanoparticles, and nanowires [42–52], magnetostriction in FeGa alloys

[53], electric-field-induced magnetization in multiferroics [54], magnetization reversal in magnetic recording media [55] and exchange-bias materials [56], and chiral and skyrmion-like structures in single crystals [57–59].

Necessary prerequisite for the quantitative analysis of elastic magnetic SANS data is the knowledge of the Fourier components of the static magnetization vector field $\mathbf{M}(\mathbf{r})$ of the sample under study. The theory of micromagnetics [60–62] provides the proper framework for the computation of $\mathbf{M}(\mathbf{r})$. However, the solution of Brown’s equations of micromagnetics amounts to the solution of a set of nonlinear partial differential equations with complex boundary conditions, a task which cannot be done analytically for most practically relevant problems. Therefore, closed-form expressions for the ensuing so-called spin-misalignment scattering cross section are limited to the approach-to-saturation regime [31, 63], in which the micromagnetic equations can be linearized.

In this review article we summarize our recent work, in which we have used *numerical* micromagnetics for the computation of the magnetic SANS cross section of two-phase magnetic nanocomposites. The use of numerical techniques allows us to solve the underlying equations rigorously, without resorting to the high-field approximation (saturation regime). This approach provides insights into the fundamentals of magnetic SANS. The micromagnetic simulations are adapted to the mi-

*Corresponding author

Email address: andreas.michels@uni.lu (Andreas Michels)

crostructure of a two-phase nanocomposite from the NANOPERM family of alloys [64]

The paper is organized as follows: in Sec. 2 we provide the details of our micromagnetic methodology, Sec. 3 discusses the magnetic SANS cross sections for the two most commonly used scattering geometries, Sec. 4 presents and discusses the results of the micromagnetic simulations for the magnetic SANS cross section, and in Sec. 5 we summarize the main findings of this study.

2. Micromagnetic background

Micromagnetism is a mesoscopic phenomenological theory designed to compute the equilibrium magnetization state of an arbitrarily shaped ferromagnetic body, when the applied field, the geometry of the ferromagnet and all materials parameters are known [60–62]. In order to find the equilibrium magnetization configuration $\mathbf{M}_{\text{eq}}(\mathbf{r})$, the total magnetic free energy of a ferromagnet should be considered as a functional of its magnetization state, $E_{\text{tot}} = E_{\text{tot}}[\mathbf{M}(\mathbf{r})]$. The state $\mathbf{M}(\mathbf{r})$ which delivers a (local) minimum to this functional corresponds to the required equilibrium magnetization configuration, so that the problem amounts to the minimization of the total energy functional. In the most common case E_{tot} contains contributions from the energy due to an external field, exchange, anisotropy and magnetodipolar interaction energies. Due to the nonlocal nature of the magnetodipolar interaction, almost all practically interesting problems can not be treated analytically, so that numerical minimization of $E_{\text{tot}}[\mathbf{M}(\mathbf{r})]$ should be carried out. In the contemporary research landscape, numerical micromagnetics is a large and still continuously expanding field. Recent reviews on the micromagnetic state of the art can be found in the handbook Ref. [65]. In this article we briefly discuss only those methodical aspects of numerical micromagnetics which are important for simulations of nanocomposite materials.

First, we would like to emphasize that such materials are one of the most complicated objects from the point of view of numerical simulations. The main difficulty is that they consist of at least two phases, and the boundaries between these phases are complicated curved surfaces; a typical example is a hard-soft nanocomposite consisting of magnetically hard (i.e., having a large magnetocrystalline anisotropy) crystal grains surrounded by a magnetically soft matrix. Such a system is very difficult to simulate for the following reasons. The majority of modern numerical micromagnetic methods can be subdivided into two classes, the so-called finite-difference and finite-element methods (FDM and FEM)

[65]. In FDM the system under study is discretized into a regular translationally invariant (usually rectangular) grid. Such a discretization allows, first, the evaluation of the exchange field by simple finite-difference formulas, which are the finite-difference approximations for the corresponding second-order differential operator acting on the magnetization field $\mathbf{M}(\mathbf{r})$ (see below). Second, the translational invariance of a FDM grid enables the usage of the fast Fourier transformation (FFT) technique for the computation of the long-range magnetodipolar interaction field and energy. For a system discretized into N cells, the FFT technique reduces the operation count for this energy from $\sim N^2$ (for a direct summation) to $\sim N \log N$. However, a serious disadvantage of a regular grid is a pure approximation for arbitrarily curved surfaces and boundaries. This is an important drawback for simulations of magnetic nanocomposites, because the adequate representation of the interphase boundaries for the accurate evaluation of associated exchange and magnetodipolar interactions between different phases is crucially important.

The second group of numerical methods widely used in micromagnetics—finite-element methods (FEM)—employ the discretization of the system under study into arbitrarily shaped tetrahedrons. The flexibility of this discretization type allows one to represent curved boundaries (including those between magnetically hard inclusions and the soft magnetic matrix) with any desired accuracy. However, the price to pay for this flexibility is high. First, computation of the exchange field requires now complicated methods designed for the accurate representation of second-order differential operators on irregular lattices. Second (and most important), it is no longer possible to use FFT for the magnetodipolar field evaluation. For this reason, highly sophisticated methods for the computation of this field are used in FEM simulations. These methods, which are based on the decomposition of magnetic potentials inside the ferromagnet and in the outer space, and the subsequent solution of the corresponding Poisson equations for these potentials on irregular grids [65] require a high programming effort and result in *iterative* algorithms for the evaluation of the dipolar field for a given magnetization configuration (in contrast to the FFT technique).

Another important limitation of finite-element methods is that they can only be employed in simulations with *open* boundary conditions (OBC), so that *periodic* boundary conditions (or PBC, routinely applied in simulations of extended thin films and bulk materials in order to eliminate strong finite-size effects) can not be used. The impossibility to apply PBC is a serious disadvantage in simulations of SANS experiments on nanocom-

posites, whereby the scattering intensity is sensitive to magnetization fluctuations in the bulk. Artificial surface demagnetizing effects arising in simulations with OBC might be very significant in this case, due to a relatively small simulation volume affordable even for modern computers. In addition, the suppression of these effects is especially important for nanocomposites containing a soft magnetic phase.

Another undesirable feature of a tetrahedron mesh is that hard magnetic grains must also be discretized into tetrahedrons, although in many cases the magnetization within a single grain is nearly homogeneous. This leads to a significant increase of the total number of finite elements required, resulting in a corresponding increase of the computation time; we refer the reader to Ref. [66] for the discussion of this problem.

Due to all the reasons explained above, numerical micromagnetic simulations of SANS experiments on nanocomposites are very rare [67, 68]. Corresponding full-scale simulations of SANS measurements on a two-phase system have been reported, up to our knowledge, only in Ref. [67], where the magnetization configuration of a longitudinal magnetic recording media film was modeled. Based on the experimental characterization of this material, the authors of [67] have built a two-phase model for this system, where each magnetic grain consisted of a hard magnetic grain core and an essentially paramagnetic grain shell, having a very high susceptibility. The OOMMF code employing the standard FDM has been used [69], so that a very fine discretization ($0.3 \times 0.3 \times 0.3 \text{ nm}^3$ cells) had to be applied in order to reproduce the spherical shape of grain cores with a required accuracy. For this reason, only a rather limited number of grains (~ 50) could be simulated. In addition, the exchange interaction both between the grains and within the soft magnetic matrix (represented by the merging grain shells) was neglected. Still, using several adjustable parameters, a satisfactory agreement of the simulated SANS intensity profile with experimental data was achieved.

The brief overview of the methodical problems presented here clearly shows that both a qualitative improvement of the micromagnetic simulation methodology and extensive numerical studies devoted to SANS experiments are highly desirable.

2.1. New micromagnetic algorithm: mesh generation and its regular representation

For the reasons explained in the previous section and in order to perform accurate and efficient simulations of two-phase nanocomposites, we need to generate a polyhedron mesh with the following properties: (a) it should

allow to represent each hard magnetic crystallite as a single finite element (because the magnetization inside such a crystallite is essentially homogeneous), (b) the mesh should allow for an arbitrarily fine discretization of the soft magnetic matrix in-between the hard grains (to account for the possible large variations of the magnetization direction between the hard grains), and (c) the shape of the meshing polyhedrons should be as close as possible to spherical, in order to ensure a good quality of a spherical dipolar approximation for the calculation of the magnetodipolar interaction energy, even for the nearest neighboring mesh elements.

A mesh consisting of polyhedrons satisfying all these requirements can be generated using two kinds of methods. First, there exist various modifications of a purely geometrical algorithm designed to obtain a random close packing of hard spheres [70]. In these algorithms, the initial distribution of sphere centers is completely random. Then, at each step the worst overlap between two spheres is eliminated by pushing these spheres apart along the line connecting their centers. This procedure usually introduces new overlaps; however, these overlaps are usually smaller and are eliminated during the next steps, so that on the average the packing quality improves (the largest overlap present in the system decreases). The algorithm is robust and produces a random close packing of nonoverlapping spheres with any desired accuracy (see Ref. [70] for further details). Unfortunately, the computation time for this method increases with the number of elements N as $\sim N^2$, so that the maximal number of spheres which can be positioned within a reasonable computation time is $N \sim 10^4$.

Therefore, in order to generate a mesh with a much larger number of finite elements ($N > 10^5$), we have developed a “physical” method, where we model a system of spheres interacting via a short-range repulsive potential:

$$U_i = \sum_{j=1}^N A_{\text{pot}} \exp \left\{ -\frac{d_{ij} - (r_i + r_j)}{r_{\text{dec}}} \right\} \quad (1)$$

Here, the constant A_{pot} determines the value of our potential when the distance d_{ij} between the centers of interacting spheres is equal to the sum of their radii r_i and r_j (to ensure small overlaps in the final configuration, it should be $A_{\text{pot}} \gg 1$; in a typical case $A_{\text{pot}} = 10$). The parameter r_{dec} defines the decay radius of the potential. Again, at the beginning of iterations, sphere centers are positioned randomly. Then, we move the spheres according to the purely dissipative (i.e., neglecting the inertial term) equation of motion resulting from the forces obtained from the potential Eq. (1). The time

254 step for the integration of this equation is adjusted to
 255 ensure decrease of the total system energy after each
 256 step. Due to the repulsive nature of the potential Eq. (1),
 257 this procedure leads also to the decrease of overlaps of
 258 the spheres. To achieve the desired result, we move the
 259 spheres until their maximum overlap does not exceed
 260 some prescribed small value (we have found that for
 261 our purposes the remaining overlap $(r_i + r_j)/d_{ij} > 0.95$
 262 is good enough). The algorithm may be refined further
 263 to increase its efficiency; in particular, one might de-
 264 crease the decay radius of the potential r_{dec} , thus mak-
 265 ing the potential “harder”, when the overlapping be-
 266 tween spheres decreases during the sphere motion. We
 267 also note that due to the random spatial arrangement of
 268 spheres obtained in this way, we avoid possible artifacts
 269 caused by the regular placement of finite elements.

270 After the spheres have been positioned using one of
 271 the two algorithms described above, their centers are
 272 used as location points of magnetic dipoles. To compute
 273 the magnitudes μ_i of these dipoles, we have to determine
 274 the volume of each corresponding mesh element, which
 275 is in fact a polyhedron. This determination is made via a
 276 regular grid representation procedure that should satisfy
 277 the following requirements. First, we should conserve
 278 the total sample volume. Second, the interface between
 279 neighboring mesh elements should be flat as far as pos-
 280 sible (apart from geometrical reasons). The last require-
 281 ment is also supported by electron microscopy images
 282 of various polycrystalline magnets (e.g., [71, 72]).

283 In order to satisfy both these requirements, we used
 284 the following method: the sample is divided into cubi-
 285 cal cells which side is much smaller (usually about four
 286 times smaller) than the size of a finite element (polyhe-
 287 dron) of our disordered mesh used to discretize the soft
 288 phase. For every cubical cell (j, k, l) , we calculate the
 289 distances $\Delta s_{j,k,l}^i$ between the center of this cell and the
 290 centers of neighboring polyhedrons (labeled by i). The
 291 function

$$292 \quad \min_{(i)} \left[(\Delta s_{j,k,l}^i)^2 - R_i^2 \right] \quad (2)$$

293 indicates to which polyhedron (with radius R_i) we at-
 294 tribute the current (j, k, l) cube. The sum of cube vol-
 295 umes ascribed to the given polyhedron is taken as its
 296 volume. As a result of this procedure, the distribu-
 297 tion of mesh-element volumes for both magnetic phases
 298 demonstrates a nearly Gaussian behavior. To obtain the
 299 magnitude of the dipolar moment assigned to each poly-
 300 hedron, its volume is multiplied by the saturation mag-
 301 netization of the material inside which the polyhedron is
 302 located (we remind that nanocomposites consist of ma-
 303 terials with different magnetizations).

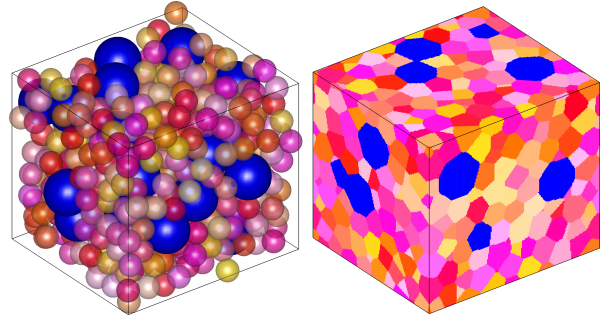


Figure 1: Schematic representation of the mesh-generation method: spheres in the left image indicate the distribution of magnetic dipoles (blue—hard magnetic phase, yellow-orange-red—soft magnetic phase). The corresponding regular grid representation on the right is used for the mesh-element volume determination (see Sec. 2.1 for details). Note that the actual “sample”, which is used for the micromagnetic simulations, is featured in Fig. 3.

304 This method also allows for a very efficient calcula-
 305 tion of the Fourier components of the magnetization
 306 (see Eqs. (17) and (18) below) for a disordered system,
 307 using FFT on the already composed regular grid.

308 Summarizing, the whole algorithm can be viewed as
 309 a method to discretize a sample into polyhedrons hav-
 310 ing nearly spherical shape (see Fig. 1). This is due to
 311 the fact that polyhedrons “inherit” the spatial structure
 312 obtained by the positioning of closely packed spheres.
 313 The fact that the shape of the volume which is occupied
 314 by each magnetic moment is nearly spherical allows us
 315 to use the spherical dipolar approximation (equivalent
 316 to the point dipole approximation) for the evaluation of
 317 the magnetodipolar interaction between the moments.

318 Finally, we point out that both algorithms allow for
 319 the usage of polyhedrons with different sizes, if we need
 320 different meshing on different system locations.

321 2.2. New micromagnetic algorithm: energy contribu- 322 tions

323 In our micromagnetic simulations we take into ac-
 324 count all four standard contributions to the total mag-
 325 netic free energy listed above: energy in the exter-
 326 nal magnetic field, energy of the magnetocrystalline
 327 anisotropy, exchange stiffness and magnetodipolar in-
 328 teraction energies.

329 2.2.1. External field and magnetocrystalline anisotropy 330 energies

331 The system energy due to the presence of an ex-
 332 ternal field and the energy of the magnetocrystalline

anisotropy (which can be uniaxial and/or cubic) are calculated in our model in the standard way, namely

$$E_{\text{ext}} = - \sum_{i=1}^N \boldsymbol{\mu}_i \mathbf{H}_{\text{ext}}, \quad (3)$$

$$E_{\text{an}}^{\text{un}} = - \sum_{i=1}^N K_i^{\text{un}} V_i (\mathbf{m}_i \mathbf{n}_i)^2, \quad (4)$$

$$E_{\text{an}}^{\text{cub}} = \sum_{i=1}^N K_i^{\text{cub}} V_i \left(m_{i,x}^2 m_{i,y}^2 + m_{i,y}^2 m_{i,z}^2 + m_{i,x}^2 m_{i,z}^2 \right),$$

where \mathbf{H}_{ext} is the external field, $\boldsymbol{\mu}_i$ and V_i are the magnetic moment and the volume of the i th finite element (polyhedron), and \mathbf{m}_i denotes the unit magnetization vector. Both the anisotropy constants K_i and the directions of the anisotropy axes \mathbf{n}_i can be site-dependent, as required for a polycrystalline nanocomposite material. For the cubic anisotropy case, the symbols $m_{i,x}$ etc. represent the components of unit magnetization vectors in the local coordinate system that is attached to the cubic anisotropy axes.

2.2.2. Exchange energy

The evaluation of this energy contribution in our model requires a much more sophisticated approach than in the standard FDM, because the continuous integral version of this energy contains the magnetization gradients,

$$E_{\text{exch}} = \int_V A(\mathbf{r}) \left[(\nabla m_x)^2 + (\nabla m_y)^2 + (\nabla m_z)^2 \right] dV, \quad (6)$$

where A denotes the exchange-stiffness parameter and V is the sample volume. Finding an approximation to Eq. (6) for a disordered system is a highly nontrivial task.

We remind that for a regular cubic grid with a cell size a (and cell volume $\Delta V = a^3$), it can be shown rigorously (see the detailed proof in Ref. [73]) that the integral in Eq. (6) can be approximated as the sum

$$E_{\text{exch}} = - \frac{1}{2} \sum_{i=1}^N \sum_{j \in \text{n.n.}(i)} \frac{2A_{ij} \Delta V}{a^2} (\mathbf{m}_i \mathbf{m}_j). \quad (7)$$

Here, A_{ij} denotes the exchange-stiffness constant between cells i and j , and the notation $j \in \text{n.n.}(i)$ means that the inner summation is performed over the nearest neighbors of the i th cell only. We note in passing that

this Heisenberg-like expression is valid only when the angles between neighboring moments are not too large; as shown in Ref. [73], neglecting this condition can lead to completely unphysical results.

For a disordered system of finite elements having different volumes, different distances between the element centers, and different numbers of nearest neighbors for each element, the expression Eq. (7) obviously can not be used. The most straightforward way to compute the exchange interaction in such a system would be to employ a rigorous numerical approximation suitable for the evaluation of the integral Eq. (6), where the integrand values (magnetization vectors \mathbf{m}) are given at arbitrarily placed spatial points. Derivation of such integration formulas amounts to the approximation of the magnetization projections $m_{x(y,z)}(\mathbf{r})$ using some kind of a polynomial interpolation of these functions between the points where their values are defined (in our case, polyhedron centers). The integrand in Eq. (6) includes first spatial derivatives of the magnetization field, so that corresponding polynomials for the energy evaluation should deliver a continuous (and even better smooth) first derivative of $\mathbf{m}(\mathbf{r})$. For the effective field evaluation, where the continuous expression involves second-order derivatives, the polynomial interpolation is even more demanding. In addition, we should keep in mind that the condition $|\mathbf{m}(\mathbf{r})| = 1$ must be fulfilled everywhere, so that the interpolation of the magnetization angles, rather than that of Cartesian magnetization components should be used. All these features would result in a highly complicated algorithm for the exchange energy and field evaluation, which might be, in addition, subject to serious stability problems to usage of the angle interpolation.

For these reasons, we have decided to develop an algorithm for the exchange-energy evaluation based on the summation of the nearest neighbors contributions [similar to the expression (Eq. 7)] and at the same time take into account the differences between a regular grid and a disordered system mentioned above. To achieve this goal, we modify the expression Eq. (7) in the following way. First, from the derivation of the expression Eq. (7) presented in [73], it is clear that for the regular mesh consisting of cubic cells, the volume ΔV in the numerator of this expression is actually not the volume of the cell, but the volume enclosed between the centers of the cell i and the neighboring cell j (for a cubic lattice or a lattice consisting of rectangular prisms, this volume is obviously equal to the cell volume, because it includes two halves of identical cells). Therefore, for a disordered system of arbitrary finite elements, ΔV should be replaced by $\bar{V}_{ij} = (V_i + V_j)/2$, where V_i and V_j are the

413 volumes of the i th and the j th finite elements.

414 The second adjustment of Eq. (7) to a finite element 463
 415 system is the replacement of the distance a between the 464
 416 cell centers in a regular lattice by the distance Δr_{ij} be- 465
 417 tween the centers of cells i and j . 466

418 The third and most complicated correction is due to 467
 419 the different number of nearest neighbors in a regular 468
 420 lattice and in a disordered system of finite elements. In 469
 421 a regular Cartesian lattice, each cell has exactly $N_{\text{nn}} = 6$ 470
 422 nearest neighbors, and the angles between the lines con- 471
 423 necting the cell center with the centers of its neighbors 472
 424 in x , y and z directions are always 90° . For this reason, 473
 425 the overlapping of volumes enclosed between the 474
 426 centers of neighboring cells in, e.g., x and y directions 475
 427 is the same for all cells, what was taken into account 476
 428 by derivation of Eq. (7) (it is important to note, that 477
 429 this overlapping should not be confused with the over- 478
 430 lapping of spheres mentioned in the discussion of algo-
 431 rithms used to construct our disordered mesh in Sec. 2.1).
 432 In contrast to this nice feature of a regular Cartesian lat-
 433 tice, in a disordered system of finite elements the num-
 434 ber of nearest neighbors for different finite elements
 435 may be different, and the overlapping of volumes en-
 436 closed between the centers of a given cell and its differ-
 437 ent neighbors may also vary. For example, for the ele-
 438 ment with more than six nearest neighbors, the volumes
 439 enclosed between its center and centers of its neighbors
 440 would overlap more than for a cubic lattice. For such
 441 an element, the exchange-stiffness energy evaluated us-
 442 ing the sum Eq. (7) would be overestimated due to this
 443 excessive overlapping, even when the two corrections
 444 explained above would be taken into account.

445 The simplest method to solve this problem is the in-
 446 troduction of the correction factor $6/n_{\text{av}}$, where n_{av}
 447 is the average number of nearest neighbors for the partic-
 448 ular random realization of our disordered finite-element
 449 system. This correction would compensate on average
 450 the effect of the incorrect count of overlapping re-
 451 gions explained above. The accuracy of this simple
 452 correction method can be hardly estimated in advance,
 453 but both simple tests performed in [74] and additional
 454 much more complicated tests discussed in Sec. 2.3 be-
 455 low show that the accuracy provided by this correction
 456 method is surprisingly good.

457 Summarizing, for magnetic moments belonging to
 458 the same phase we propose the following expression for
 459 the exchange-stiffness energy:

$$460 \quad E_{\text{exch}} = -\frac{1}{2} \sum_{i=1}^N \sum_{j \in \text{n.n.}(i)} \frac{2A_{ij} \bar{V}_{ij}}{\Delta r_{ij}^2} (\mathbf{m}_i \mathbf{m}_j), \quad (8)$$

461 where $\bar{V}_{ij} = (V_i + V_j)/2$, Δr_{ij} is the distance between

462 the centers of the i th and the j th finite elements with
 463 volumes V_i and V_j , and A_{ij} is the exchange constant.

The last point to be discussed is the choice of nearest
 464 neighbors, which should be used in the inner summation
 465 in Eq. (8). The choice whether two elements should
 466 be considered as nearest neighbors is not unambiguous
 467 in disordered systems. We have adopted the following
 468 convention: two magnetic moments are considered as
 469 nearest neighbors, if the distance between the centers
 470 of corresponding polyhedrons is not larger than $d_{\text{max}} =$
 471 $1.4(r_i + r_j)$. The cut-off factor $f_{\text{cut}} = 1.4$ is chosen so that
 472 for the overwhelming majority of finite elements those
 473 two of them which have a common face are treated as
 474 nearest neighbors. 475

To evaluate the exchange-interaction energy between
 476 two finite elements (polyhedrons) belonging to *different*
 477 phases (hard and soft), we use the formula:

$$478 \quad E_{\text{exch}} = -\frac{1}{2} \sum_{i=1}^N \sum_{j \in \text{n.n.}(i)} \frac{2A_{ij} V_{\text{sp}}/2}{(\Delta r_{ij} - R_{\text{hp}})^2} (\mathbf{m}_i \mathbf{m}_j). \quad (9)$$

479 Here, V_{sp} is the volume of a soft-phase element and R_{hp}
 480 is the radius of the sphere corresponding to the hard
 481 phase polyhedron. This modified expression Eq. (9) ac-
 482 counts for the fact that in this case the magnetization
 483 rotation occurs almost entirely within the polyhedron
 484 corresponding to the soft phase. 485

486 2.2.3. Magnetodipolar interaction

487 The energy of the long-range magnetodipolar interac-
 488 tion between magnetic moments and the corresponding
 489 contribution to the total effective field are computed us-
 490 ing the point-dipole approximation as

$$491 \quad E_{\text{dip}} = -\frac{1}{2} \sum_{i=1}^N \mu_i \sum_{j \neq i} \frac{3\mathbf{e}_{ij}(\mathbf{e}_{ij} \mu_j) - \mu_j}{\Delta r_{ij}^3}, \quad (10)$$

492 i.e., magnetic moments of finite elements are treated as
 493 point dipoles located at the polyhedron centers. This ap-
 494 proximation is equivalent to the approximation of spher-
 495 ical dipoles, i.e., it would be exact for spherical finite el-
 496 ements. Hence, for our discretized system, this approx-
 497 imation introduces some computational errors, because
 498 our finite elements are polyhedrons. However, these er-
 499 rors are small, because the shape of these polyhedrons
 500 is close to spherical (see Fig. 3), due to the special al-
 501 gorithm employed for the generation of our mesh, as
 502 explained in Sec. 2.1.

The summation in Eq. (10) is performed by the so
 503 called particle-mesh Ewald method. Didactically very
 504 instructive and detailed introduction into Ewald meth-
 505 ods can be found in Ref. [75]. The specific implemen-
 506

tation of the lattice-based Ewald method for the magnetodipolar interaction for regular and disordered systems of magnetic particles is described in our papers [76, 77]. Here, we briefly repeat the basic issues of this algorithm to make our paper self-containing.

First we remind that the Ewald method [78] was initially invented for evaluating conditionally converging lattice sums for the Coulomb interaction in ionic crystals. At present, it is a standard method to calculate any long-range interaction—including Coulomb sums, gravitation energy, dipole interaction, elastic forces in dislocation networks etc.—in systems with periodic boundary conditions (PBC). In such systems direct summation over all field sources is impossible simply due to their infinite number. Hence, we must use a Fourier expansion over the reciprocal lattice vectors \mathbf{k} which correspond to the infinitely repeated simulation volume. For the *point* sources of the *long-range* field, the corresponding Fourier components decay relatively slowly with increasing magnitude of the wave vector k in reciprocal space. In numerical simulations we always have to our disposal only a finite number of such wave vectors, so that the Fourier spectrum of our long-range interaction should be cut off at the maximal finite value k_{\max} . As mentioned above, the Fourier harmonics decay slowly, so that at k_{\max} they are by no means small. For this reason, the spectrum cut-off due to the elimination of all Fourier components with $k > k_{\max}$ is sharp, thus, leading to large artificial oscillations of the interaction potential after its inverse transformation to the real space.

As with nearly all Ewald methods, the version described below for dipolar systems solves the problem by adding and subtracting a Gaussian dipole at each location of a point dipole $\boldsymbol{\mu}_i$ in the initial system. Using the definition of the gradient of the δ function, it is easy to show that this operation corresponds to the addition and subtraction of a charge distribution

$$\rho_i^G(\mathbf{r}) = -\frac{(\mathbf{r} - \mathbf{r}_i)\boldsymbol{\mu}_i}{(2\pi)^{3/2}\sigma^5} \exp\left(-\frac{(\mathbf{r} - \mathbf{r}_i)^2}{2\sigma^2}\right). \quad (11)$$

Then the magnetodipolar field $\mathbf{H}^{\text{dip}} = \mathbf{H}_A^{\text{dip}} + \mathbf{H}_B^{\text{dip}}$ is evaluated as the sum of two contributions from subsystems *A* and *B*. The first subsystem consists of Gaussian dipoles (11) and the second one is composed of the original point dipoles minus these Gaussian dipoles,

$$\rho_B(\mathbf{r}) = -\sum_{i=1}^N \left[\boldsymbol{\mu}_i \nabla \delta(\mathbf{r} - \mathbf{r}_i) - \rho_i^G(\mathbf{r}) \right], \quad (12)$$

where the first terms in the sum on the right represent the charge density of a point dipole located at \mathbf{r}_i . The

field created by a composite object in square brackets of Eq. (12) is [76]

$$H_{B,i}^\alpha(\mathbf{r} - \mathbf{r}_i) = \left[\frac{3(\alpha - \alpha_i)(\boldsymbol{\mu}_i \Delta \mathbf{r}_i)}{\Delta r_i^5} - \frac{\mu_i^\alpha}{\Delta r_i^3} \right] f_G(\Delta r_i) + \sqrt{\frac{2}{\pi}} \frac{(\alpha - \alpha_i)(\boldsymbol{\mu}_i \Delta \mathbf{r}_i)}{\Delta r_i^5} \exp\left[-\frac{\Delta r_i^2}{2\sigma^2}\right], \quad (13)$$

where $\alpha = x, y, z$.

It is important to note that the function $f_G(r)$ decays with distance as $\exp(-r^2)$,

$$f_G(r) = 1 - \operatorname{erf}\left(\frac{r}{\sigma\sqrt{2}}\right) + \frac{\sqrt{2}r}{\pi a} \exp\left[-\frac{r^2}{2\sigma^2}\right]. \quad (14)$$

The goal of this decomposition of the original system of *point* dipoles is the following. The field Eq. (13) from the second subsystem *B* is a *short-range* one, because each point dipole is screened by a Gaussian dipole with the same total moment, but with the opposite sign. The computation of such a short-range contribution takes $\sim N$ operations for a system of N particles. The first subsystem *A* consists of dipoles having a smooth Gaussian charge distribution, so that its Fourier components decay rapidly with increasing k . This fast decay allows a painless cut-off of the Fourier spectrum at large wave vectors, so that the contribution from the first subsystem Eq. (11) can be safely calculated using Fourier expansion. More detailed explanations concerning this procedure can be found in Ref. [76].

Already the above most straightforward implementation of the Ewald method allows for a reliable evaluation of the dipolar field in systems with PBC. However, for disordered systems, this method has the same prohibitively high operation count $\sim N^2$, as a direct summation for systems with OBC. The reason is that particle positions in disordered systems do not form a regular lattice, so that the Fourier transformation for the calculation of the long-range contribution $\mathbf{H}_A^{\text{dip}}$ can not be done via the *fast* Fourier transformation technique: exponential factors $\exp(i\mathbf{k}\mathbf{r}_i)$ should be computed for all wave vectors \mathbf{k} and all particle positions \mathbf{r}_i separately, leading to the operation count given above.

In order to decrease the computational costs, several lattice versions of the Ewald method have been developed (see the overview [79]). The general idea behind all these methods is to employ some mapping of the initial disordered system onto a regular lattice, in order to enable the application of the FFT. Using this general paradigm, we have implemented the following algorithm:

(i) First, we map our disordered system of point magnetic dipoles $\boldsymbol{\mu}_i = \boldsymbol{\mu}(\mathbf{r}_i)$ onto a system of dipoles located at lattice points \mathbf{r}_p (p is the 3D index) using some weighting function $w_{3d}(\mathbf{r})$,

$$\begin{aligned} \tilde{\boldsymbol{\mu}}(\mathbf{r}_p) &= \sum_{i=1}^N \boldsymbol{\mu}(\mathbf{r}_i) w_{3d}(|\mathbf{r}_i - \mathbf{r}_p|) = \\ &= \sum_{i=1}^{M_{nb}} \boldsymbol{\mu}_i w(|x_i - x_p|) w(|y_i - y_p|) w(|z_i - z_p|). \end{aligned} \quad (15)$$

We emphasize that the whole method makes only sense if the mapping function w is strongly localized, so that the sum over all N dipoles in Eq. (15) is actually restricted to a few nearest neighbors M_{nb} of the lattice node p .

(ii) Next, we add and subtract to each point lattice dipole two Gaussian dipoles Eq. (12), as in the straightforward Ewald method described above.

(iii) Further, we compute the dipolar field of this lattice system as described above, i.e., as the sum of the long-range contribution from smooth Gaussian dipoles positioned *on the lattice* and the short-range contribution Eq. (13) from the composite objects “point dipole – Gaussian dipole”, also placed on the lattice.

(iv) Finally, the field obtained in this way on the lattice points \mathbf{r}_p is mapped back onto the initial dipole locations \mathbf{r}_i using the same functions w as in Eq. (15).

As mentioned above, the major advantage of this lattice Ewald version is the possibility to use FFT for computing the long-range part of the total magnetodipolar field. In addition, we can also accelerate the evaluation of the short-range contribution. Namely, we note that (i) the contribution Eq. (13) depends only on the difference $\Delta\mathbf{r}$ between the source and target coordinates and (ii) both source and target points are located on the lattice. Hence, this short-range contribution also is a discrete convolution and as such can be also computed by the FFT technique. Using this nice feature, we can increase the number of nearest neighbor shells used by the evaluation of the short-range interaction part without additional time cost, making the corresponding truncation error arbitrarily small. Keeping in mind that the evaluation of the long-range field part via the FFT technique for the *lattice* system is exact, we conclude that the only source of computational errors in our algorithm is the mapping of the initial disordered system onto a lattice, which can be easily controlled and reduced by choosing the suitable mapping scheme [79]. We have found that already the conventional first-order mapping used together with a lattice having a cell size equal to $R_{sp}/2$ (here R_{sp} is the sphere radius used to generate the mesh

for the soft-phase discretization) ensures by the evaluation of \mathbf{H}^{dip} a relative error smaller than 0.01, which is good enough for our purposes.

2.3. New micromagnetic algorithm: minimization procedure and numerical tests

For the minimization of the total magnetic energy, obtained as the sum of all contributions described above, we use the simplified version of a gradient method employing the dissipation part of the Landau-Lifshitz equation of motion for magnetic moments [65, 80]. This means that we update the magnetization configuration at each step as

$$\mathbf{m}_i^{\text{new}} = \mathbf{m}_i^{\text{old}} - \Delta t \left[\mathbf{m}_i^{\text{old}} \times \left[\mathbf{m}_i^{\text{old}} \times \mathbf{h}_i^{\text{eff}} \right] \right], \quad (16)$$

where \mathbf{m}_i denotes the unit magnetization vector $\mathbf{m}_i = \mathbf{M}_i/M_S$ and $\mathbf{h}_i^{\text{eff}}$ is the reduced effective field, evaluated in a standard way as the negative energy derivative over the magnetic moment projections [65].

Since we are looking for the energy minimum, the time step in Eq. (16) is chosen and adapted using the monitoring of this energy. If the total energy decreases after the iteration step performed according to Eq. (16), we accept this step. If the energy increases, we restore the previous magnetization state, halve the time step ($\Delta t \rightarrow \Delta t/2$) and repeat the iteration. During the minimization procedure we may also increase the time step to avoid an unnecessary slow minimization: the time step is doubled, if the last few steps (typically 5 – 10 steps) were successful. For the termination of the minimization procedure, we use the local torque criterion: we stop the iteration process, if the maximal torque acting on magnetic moments is smaller than some prescribed value, i.e., $\max_i \{ |\mathbf{m}_i \times \mathbf{h}_i^{\text{eff}}| \} < \varepsilon$. As is well known, this condition is more appropriate than the alternative criterion of a sufficiently small energy difference between the two subsequent steps. In all tested cases the value $\varepsilon = 10^{-3}$ was small enough to ensure the minimization convergence.

The new methodology explained in detail above was tested on two simple examples in Ref. [74]. We remind that we have first reproduced—using our disordered mesh—with a high accuracy the analytically known magnetization profile of a standard 3D Bloch wall. Second, for a trial 3D magnetic configuration defined via simple trigonometric functions of coordinates (we have used these functions to ensure a sufficiently slow spatial variation of the system magnetization direction), we have obtained a very good agreement between the total energy and partial energy contributions found by our new method and the FDM micromagnetic package MicroMagus [81].

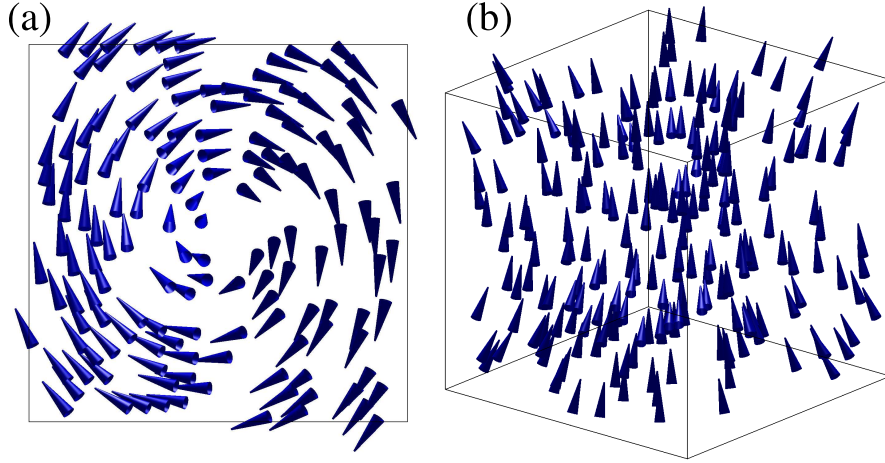


Figure 2: (a) Vortex (2D cross section) and (b) flower (3D arrow plot) magnetization states obtained by our new methodology explained in Sec. 2.3 above. Data taken from Ref. [82].

Here, we would like to present two additional much more complicated tests, where we compute the equilibrium magnetization configurations of a cubic magnetic particle obtained using our new method and compare these configurations with the results obtained for the same system by the MicroMagus package.

The particle size was chosen to be $40 \times 40 \times 40 \text{ nm}^3$, and the magnetic materials parameters were set to $M_S = 800 \text{ kA/m}$, $A = 1.0 \times 10^{-11} \text{ J/m}$, and $K = 5.0 \times 10^4 \text{ J/m}^3$ (uniaxial anisotropy). For the simulations using our new method, the particle was discretized into $N = 9000$ polyhedrons with a typical size of $d = 2 \text{ nm}$. For the MicroMagus simulations, a cubic cell with a side length of 2.5 nm was used.

For the test problems, we have chosen two well known magnetization states typical for ferromagnetic particles of this size [83]: the vortex state and the so-called flower state. To obtain the vortex state, we have started the minimization procedure from the state that is topologically equivalent to the vortex, the so-called closed Landau domain configuration. The flower state could be obtained by starting the energy minimization simply from the homogeneous configuration with the magnetization directed along a cube side.

Table 1 lists the total energies, partial energy contributions and the reduced magnetization values for the equilibrium magnetization states shown in Fig. 2 obtained by the new method and by the standard FDM simulations (MicroMagus package). Almost all energy contributions obtained by the two methods agree very well. The only significant relative difference can be found for the anisotropy energy of the flower state; however, this significant *relative* difference ($\Delta E/E$) arises

Table 1: Comparison of energies and reduced magnetizations for the vortex and flower magnetization states computed by the new method and by the standard finite difference simulations (MicroMagus software). Data taken from Ref. [82].

Vortex energies ($\times 10^{-18} \text{ J}$)	New method	MicroMagus
E_{tot}	8.225	8.270
E_{an}	1.361	1.385
E_{exch}	4.409	4.562
E_{dip}	2.455	2.324
M/M_S	0.400	0.406

Flower energies ($\times 10^{-18} \text{ J}$)	New method	MicroMagus
E_{tot}	7.813	7.843
E_{an}	0.137	0.127
E_{exch}	0.434	0.441
E_{dip}	7.242	7.275
M/M_S	0.972	0.974

simply due to a very low value of this energy. All in one, the agreement between the new and the established methodologies for all cases where the standard methods are applicable is fully satisfactory.

3. Magnetic SANS cross section of unpolarized neutrons

In our micromagnetic simulations of elastic magnetic SANS we have focussed on the two most commonly employed scattering geometries where the wavevector \mathbf{k}_0 of the incident neutron beam is either perpendicular [case (i)] or parallel [case (ii)] to the external magnetic field \mathbf{H} , which is applied along the z -direction of a Cartesian coordinate system. (\mathbf{e}_x , \mathbf{e}_y and \mathbf{e}_z represent the unit vectors along the Cartesian axes.) Furthermore, since the focus of the present study is on mag-

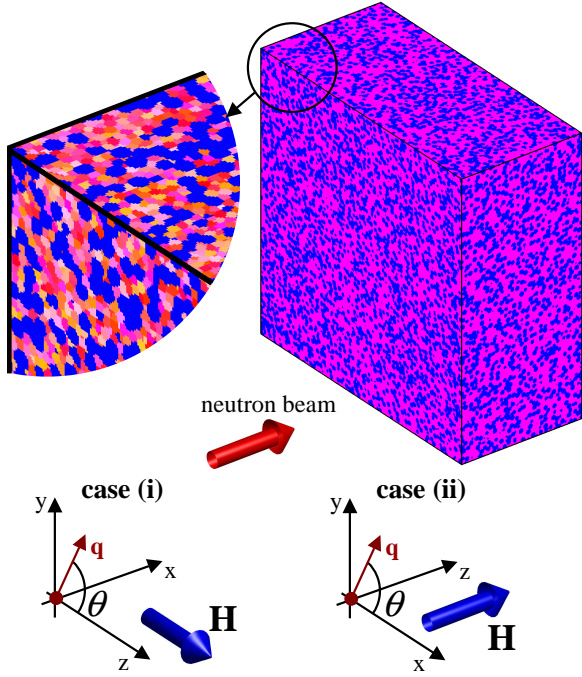


Figure 3: Sketch of the two scattering geometries and of the microscopic structure of the nanocomposite sample.

731 netic spin-misalignment scattering, we have ignored
 732 the nuclear SANS contribution. Note, however, that
 733 for polycrystalline texture-free magnetic nanocompos-
 734 ites the nuclear SANS signal is virtually independent of
 735 the applied magnetic field and isotropic, and its mag-
 736 nitude is generally small compared to the here relevant
 737 spin-misalignment scattering [31]. Furthermore, the re-
 738 striction to unpolarized neutrons entails the neglect of
 739 scattering contributions from helical spin arrangements,
 740 which are of relevance, e.g., in FeCoSi and MnSi single
 741 crystals [58, 59].

742 A sketch of the above two scattering geometries along
 743 with a schematic drawing of the microscopic structure
 744 of the nanocomposite sample can be seen in Fig. 3.

745 3.1. Case (i): $\mathbf{k}_0 \perp \mathbf{H} \parallel \mathbf{e}_z$

For $\mathbf{k}_0 \parallel \mathbf{e}_x$, the elastic magnetic SANS cross section
 $d\Sigma_M/d\Omega$ at momentum-transfer vector \mathbf{q} reads [31]

$$746 \frac{d\Sigma_M}{d\Omega}(\mathbf{q}) = \frac{8\pi^3}{V} b_H^2 \left(|\tilde{M}_x|^2 + |\tilde{M}_y|^2 \cos^2 \theta \right. \\ 747 \left. + |\tilde{M}_z|^2 \sin^2 \theta - (\tilde{M}_y \tilde{M}_z^* + \tilde{M}_y^* \tilde{M}_z) \sin \theta \cos \theta \right), \quad (17)$$

748 where $V = 250 \times 600 \times 600 \text{ nm}^3$ is the scattering vol-
 749 ume, $b_H = 2.9 \times 10^8 \text{ A}^{-1} \text{ m}^{-1}$, c^* is a quantity complex-
 748 conjugated to c , and $\tilde{M}_{(x,y,z)}(\mathbf{q})$ are the Fourier trans-
 749 forms of the magnetization components $M_{(x,y,z)}(\mathbf{r})$. Note

750 that in the small-angle limit and for this particular ge-
 751 ometry the scattering vector \mathbf{q} can be expressed as $\mathbf{q} \cong$
 752 $q(0, \sin \theta, \cos \theta)$, where θ denotes the angle between \mathbf{q}
 753 and \mathbf{H} (Fig. 3).

754 3.2. Case (ii): $\mathbf{k}_0 \parallel \mathbf{H} \parallel \mathbf{e}_z$

For this geometry, one finds

$$755 \frac{d\Sigma_M}{d\Omega}(\mathbf{q}) = \frac{8\pi^3}{V} b_H^2 \left(|\tilde{M}_x|^2 \sin^2 \theta + |\tilde{M}_y|^2 \cos^2 \theta \right. \\ 756 \left. + |\tilde{M}_z|^2 - (\tilde{M}_x \tilde{M}_y^* + \tilde{M}_x^* \tilde{M}_y) \sin \theta \cos \theta \right), \quad (18)$$

755 where $\mathbf{q} \cong q(\cos \theta, \sin \theta, 0)$ and θ is measured relative
 756 to \mathbf{e}_x (Fig. 3).

757 For the micromagnetic simulations of magnetic
 758 SANS from two-phase nanocomposites, we used (un-
 759 less otherwise stated) the following materials param-
 760 eters for hard (“h”) and soft (“s”) phases, which are
 761 characteristic for the Fe-based nanocrystalline alloy
 762 NANOPERM [64]: magnetizations $M_h = 1750 \text{ kA/m}$
 763 and $M_s = 550 \text{ kA/m}$, anisotropy constants $K_h = 4.6 \times$
 764 10^4 J/m^3 and $K_s = 1.0 \times 10^2 \text{ J/m}^3$. As a value for the
 765 exchange-stiffness constant we used $A = 0.2 \times 10^{-11} \text{ J/m}$
 766 for interactions both within the soft phase and between
 767 the hard and soft phases.

768 4. Results and discussion

769 The applied-field dependence of the total magnetic
 770 SANS cross sections $d\Sigma_M/d\Omega$ [computed, respectively,
 771 by means of Eqs. (17) and (18)] is displayed in Fig. 4
 772 for both scattering geometries, i.e., for the situations when
 773 the wavevector \mathbf{k}_0 of the incoming neutron beam is per-
 774 pendicular [case (i)] or parallel [case (ii)] to the applied
 775 magnetic field \mathbf{H} , which for both cases is assumed to be
 776 parallel to \mathbf{e}_z . The corresponding radially-averaged data
 777 can be seen in Fig. 5.

778 While $d\Sigma_M/d\Omega$ for $\mathbf{k}_0 \parallel \mathbf{H}$ is isotropic (i.e., θ inde-
 779 pendent) over the whole field and momentum-transfer
 780 range, it is highly anisotropic for $\mathbf{k}_0 \perp \mathbf{H}$ (Fig. 4). At
 781 a saturating applied magnetic field of $\mu_0 H = 1.5 \text{ T}$,
 782 where the normalized “sample” magnetization is (for
 783 both geometries) larger than 99.9%, the anisotropy of
 784 $d\Sigma_M/d\Omega$ [case (i)] is clearly of the $\sin^2 \theta$ -type, i.e., elon-
 785 gated normal to \mathbf{H} ; this is because magnetic scattering
 786 due to transversal spin misalignment is small close to
 787 saturation and the dominating scattering contrast arises
 788 from nanoscale jumps of the longitudinal magnetiza-
 789 tion at phase boundaries. On decreasing the field, the
 790 transversal magnetization components increase in mag-
 791 nitude as long-range spin misalignment develops at the
 792 smallest q . The SANS pattern in case (i) essentially

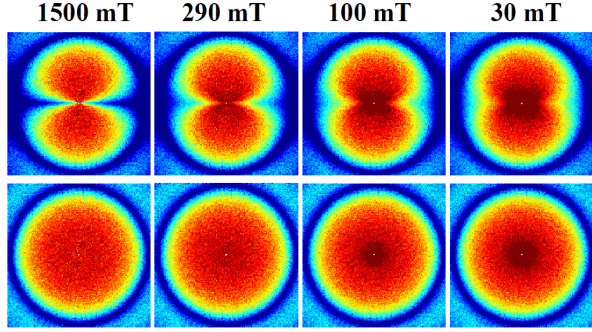


Figure 4: Applied-field dependence of the total magnetic SANS cross section $d\Sigma_M/d\Omega$ for $\mathbf{k}_0 \perp \mathbf{H}$ (Eq. (17), upper row) and for $\mathbf{k}_0 \parallel \mathbf{H}$ (Eq. (18), lower row). The external magnetic field $\mathbf{H} \parallel \mathbf{e}_z$ is applied horizontally in the plane of the detector for $\mathbf{k}_0 \perp \mathbf{H}$ (upper row) and normal to the detector plane for $\mathbf{k}_0 \parallel \mathbf{H}$ (lower row). Materials parameters of NANOPERM were used (see text). Pixels in the corners of the images have $q \cong 1.2 \text{ nm}^{-1}$. Logarithmic color scale is used.

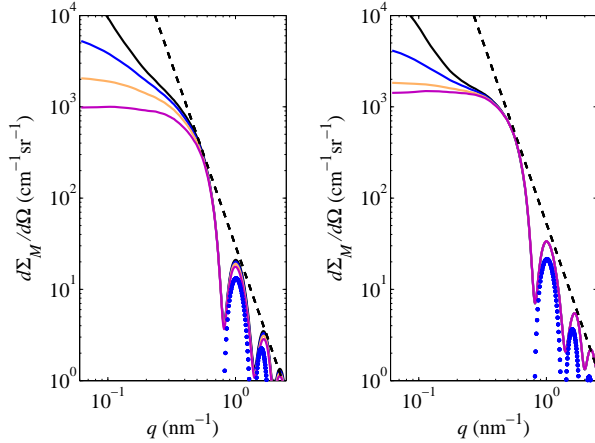


Figure 5: Solid lines: Radially-averaged $d\Sigma_M/d\Omega$ as a function of scattering vector q for $\mathbf{k}_0 \perp \mathbf{H}$ (left image) and for $\mathbf{k}_0 \parallel \mathbf{H}$ (right image) (data have been smoothed). Field values (in mT) from top to bottom, respectively: 30, 100, 290, 1500. Dashed lines in both images: $d\Sigma_M/d\Omega \propto q^{-4}$. Solid circles in both images represent part of the form factor of a sphere with a radius of $R = 5.7 \text{ nm}$.

793 remains of the $\sin^2 \theta$ -type at lower fields, although a
 794 more complicated anisotropy builds up at small q . As
 795 can be seen in Fig. 5, $d\Sigma_M/d\Omega$ at small q increases by
 796 more than order of magnitude as the field is decreased
 797 from 1.5 T to 30 mT. Asymptotically, at large q , the
 798 power-law dependence of $d\Sigma_M/d\Omega$ can be described by
 799 $d\Sigma_M/d\Omega \propto q^{-4}$. In agreement with the uniform nature
 800 of the underlying microstructure (homogeneous 11 nm-
 801 sized particles in a homogeneous matrix), one can de-
 802 scribe the oscillations of $d\Sigma_M/d\Omega$ at large q by the form
 803 factor of a sphere with a radius of $R = 5.7 \text{ nm}$ (solid
 804 circles in Fig. 5).

805 Figure 6 shows the projections of the magnetization
 806 Fourier coefficients $|\tilde{M}_x|^2$, $|\tilde{M}_y|^2$, $|\tilde{M}_z|^2$, and of the cross
 807 terms $CT = -(\tilde{M}_y \tilde{M}_z^* + \tilde{M}_y^* \tilde{M}_z)$ and $CT = -(\tilde{M}_x \tilde{M}_y^* +$
 808 $\tilde{M}_x^* \tilde{M}_y)$ into the plane of the two-dimensional detec-
 809 tor at the same external-field values as in Fig. 4. It
 810 can be seen in Fig. 6 that in case (i) both $|\tilde{M}_x|^2$ and
 811 $|\tilde{M}_z|^2$ are isotropic over the displayed (q, H) range, while
 812 the Fourier coefficient $|\tilde{M}_y|^2$ reveals a pronounced an-
 813 gular anisotropy, with maxima that lie roughly along
 814 the diagonals of the detector (the so-called “clover-leaf”
 815 anisotropy, see Fig. 10 below). In case (ii), $|\tilde{M}_x|^2$ and
 816 $|\tilde{M}_y|^2$ are both strongly anisotropic (with characteristic
 817 maxima in the plane perpendicular to \mathbf{H}), while $|\tilde{M}_z|^2$ is
 818 isotropic. When [for case (ii)] all Fourier coefficients
 819 are multiplied by the corresponding trigonometric func-
 820 tions and summed up [compare Eq. (18)], the resulting
 821 $d\Sigma_M/d\Omega$ becomes isotropic (Fig. 4, lower row).

822 The cross terms for both scattering geometries vary
 823 in sign between quadrants on the detector. The respec-
 824 tive CT is positive in the upper right quadrant of the
 825 detector ($0^\circ < \theta < 90^\circ$), negative in the upper left quad-
 826 rant ($90^\circ < \theta < 180^\circ$), and so on. When both CT 's
 827 are multiplied by $\sin \theta \cos \theta$, the corresponding contri-
 828 bution to $d\Sigma_M/d\Omega$ becomes positive-definite for all an-
 829 gles θ . This observation suggests that—contrary to the
 830 common assumption that the CT averages to zero for
 831 statistically isotropic polycrystalline microstructures—
 832 the CT appears to be of special relevance in nanocom-
 833 posite magnets.

834 In Fig. 7 we show for both scattering geometries
 835 the radially-averaged total $d\Sigma_M/d\Omega$ along with the
 836 radially-averaged *individual* scattering contributions to
 837 $d\Sigma_M/d\Omega$, i.e., the radial average of terms $\frac{8\pi^3}{V} b_H^2 |\tilde{M}_x|^2$,
 838 $\frac{8\pi^3}{V} b_H^2 |\tilde{M}_y|^2 \cos^2 \theta$, $\frac{8\pi^3}{V} b_H^2 CT \sin \theta \sin \theta$, and so on [com-
 839 pare Eqs. (17) and (18)]. At saturation ($\mu_0 H = 1.5 \text{ T}$),
 840 both transversal scattering contributions, i.e., terms \propto
 841 $|\tilde{M}_x(q)|^2$ and $\propto |\tilde{M}_y(q)|^2$, are for both cases (i) and (ii)
 842 small relative to the other terms and the main contribu-
 843 tion to the total $d\Sigma_M/d\Omega$ originates from longitudinal
 844 magnetization fluctuations, i.e., from terms $\propto |\tilde{M}_z(q)|^2$
 845 and $\propto |\tilde{M}_z(q)|$ [the CT for case (i)]. For $\mathbf{k}_0 \parallel \mathbf{H}$, both
 846 transversal terms are so small that they are not visi-
 847 ble within the displayed “intensity” range and $d\Sigma_M/d\Omega$
 848 practically equals the $|\tilde{M}_z(q)|^2$ scattering (both curves
 849 superimpose). Note that the CT for case (i) is the prod-
 850 uct of a transversal and the longitudinal magnetization
 851 Fourier coefficient, whereas for case (ii) the CT contains
 852 the two transversal components. This explains why the
 853 CT for case (ii) is much smaller than the CT for case (i)
 854 at fields close to saturation. On decreasing the field,
 855 the transversal Fourier coefficients and the CT 's become

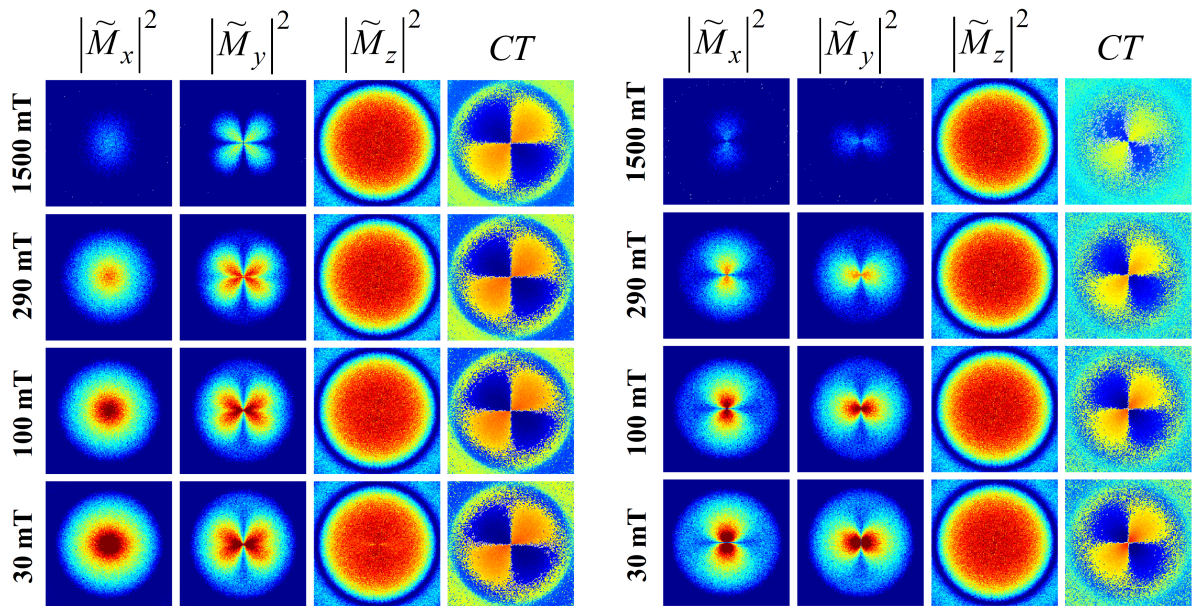


Figure 6: Results of the micromagnetic simulations for the Fourier coefficients of the magnetization. The images represent projections of the respective functions into the plane of the two-dimensional detector, i.e., $q_x = 0$ for $\mathbf{k}_0 \perp \mathbf{H}$ (left image) and $q_z = 0$ for $\mathbf{k}_0 \parallel \mathbf{H}$ (right image). From left column to right column, respectively: $|\tilde{M}_x|^2$, $|\tilde{M}_y|^2$, $|\tilde{M}_z|^2$, and $CT = -(\tilde{M}_y \tilde{M}_z^* + \tilde{M}_y^* \tilde{M}_z)$ (left image) and $CT = -(\tilde{M}_x \tilde{M}_y^* + \tilde{M}_x^* \tilde{M}_y)$ (right image). In the first three columns from left, red color corresponds, respectively, to “high intensity” and blue color to “low intensity”; in the fourth column, blue color corresponds to negative and orange-yellow color to positive values of the CT . All other settings are as in Fig. 4.

856 progressively more important, in particular at small q .

857 It is also important to note that the present simulations were carried out by assuming a quite large jump
 858 in the magnetization magnitude ΔM at the interphase between particles and matrix, $\mu_0 \Delta M = 1.5$ T. Conse-
 859 quently, the ensuing $|\tilde{M}_z(q)|^2$ scattering in both geometries and the CT scattering in case (i) are relatively large.
 860 For $\Delta M = 0$, the CT at saturation for case (i) becomes
 861 negligible, since $\tilde{M}_z(\mathbf{q}) \propto \delta(\mathbf{q} = 0)$.
 862
 863
 864

865 Figures 6 and 7 embody the power of our approach:
 866 By employing numerical micromagnetics for the com-
 867 putation of magnetic SANS cross sections, it becomes
 868 possible to study the *individual* magnetization Fourier
 869 coefficients and their contribution to $d\Sigma_M/d\Omega$. This
 870 sheds light on the ongoing discussion regarding the
 871 explicit \mathbf{q} -dependence of $d\Sigma_M/d\Omega$ [56]. In particu-
 872 lar, the approach of combining micromagnetics and
 873 SANS complements neutron experiments, which gener-
 874 ally provide only a weighted sum of Fourier coefficients
 875 [compare Eqs. (17) and (18)], a fact that often hampers
 876 the straightforward interpretation of recorded SANS
 877 data. While it is in principle possible to determine some
 878 Fourier coefficients, e.g., through the application of a
 879 saturating magnetic field or by exploiting the neutron-
 880 polarization degree of freedom via so-called SANSPOL
 881 or POLARIS methods (e.g., Refs. [18, 51, 84]), it is

882 often difficult to unambiguously determine a particu-
 883 lar scattering contribution without “contamination” by
 884 unwanted Fourier components. For instance, when the
 885 applied field is not large enough to completely saturate
 886 the sample, then the scattering of unpolarized neutrons
 887 along the field direction does not represent the pure nu-
 888 clear SANS, but contains also the magnetic SANS due
 889 to the misaligned spins [39].

890 The finding [for case (i)] that $|\tilde{M}_x|^2$ and $|\tilde{M}_z|^2$ are
 891 isotropic and that $|\tilde{M}_y|^2 = |\tilde{M}_y|^2(q, \theta)$ provides a straight-
 892 forward explanation for the experimental observation
 893 of the clover-leaf anisotropy in the SANS data of
 894 the nanocrystalline two-phase alloy NANOPERM [17].
 895 Our simulation results for the difference cross section
 896 $\propto (|\tilde{M}_x|^2 + |\tilde{M}_y|^2) \cos^2 \theta + CT \sin \theta \cos \theta$ (see Figs. 8
 897 and 9), where the scattering at saturation ($\mu_0 H = 1.5$ T) has
 898 been subtracted, agree qualitatively well with the ex-
 899 perimental data [74, 82]. Clover-leaf-type anisotropies
 900 in $d\Sigma_M/d\Omega$ have also been reported for a number of
 901 other materials, including precipitates in steels [39],
 902 nanocrystalline Gd [32, 35], and nanoporous Fe [33].
 903

904 The maxima in the difference cross section [for
 905 case (i)] depend on q and H , and may appear at angles θ
 906 significantly smaller than 45° . This becomes evident in
 907 Fig. 10, where we show (for $\mathbf{k}_0 \perp \mathbf{H}$) polar plots of the

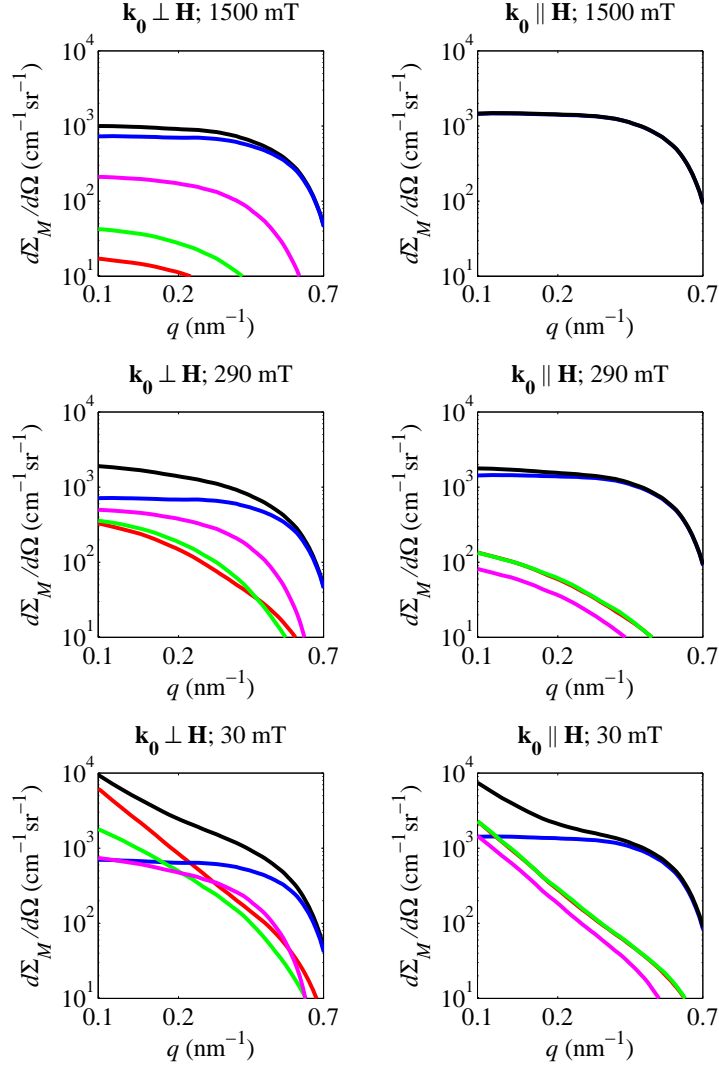


Figure 7: Radially-averaged total magnetic SANS cross sections $d\Sigma_M/d\Omega$ and radially-averaged individual contributions to $d\Sigma_M/d\Omega$ as a function of scattering vector q and applied magnetic field H for $\mathbf{k}_0 \perp \mathbf{H}$ and $\mathbf{k}_0 \parallel \mathbf{H}$ (see insets). Black lines: total $d\Sigma_M/d\Omega$; Blue lines: $|\widetilde{M}_y|^2$; Magenta lines: CT ; Green lines: $|\widetilde{M}_y|^2$; Red lines: $|\widetilde{M}_x|^2$. In the above notation, the prefactor $\frac{8\pi^3}{V}b_H^2$ and the numerical factors that result from the averaging procedure have been omitted for clarity. Note that different trigonometric functions may be involved in the averaging procedure, compare, e.g., $\frac{8\pi^3}{V}b_H^2|\widetilde{M}_x|^2$ for $\mathbf{k}_0 \perp \mathbf{H}$ [Eq. (17)] and $\frac{8\pi^3}{V}b_H^2|\widetilde{M}_x|^2 \sin^2 \theta$ for $\mathbf{k}_0 \parallel \mathbf{H}$ [Eq. (18)].

908 simulated difference cross section at selected q and H .

909 The results of our previous work [82, 85] strongly
 910 suggest that the magnetodipolar interaction plays a decisive
 911 role for the understanding of magnetic SANS of
 912 nanocomposites. In fact, it is this interaction which is
 913 responsible for the anisotropy, i.e., for the θ -dependence
 914 of the magnetization Fourier coefficients and, hence,
 915 of $d\Sigma_M/d\Omega$. The impact of the dipolar interaction on
 916 $d\Sigma_M/d\Omega$ can be conveniently studied, since our micro-
 917 magnetic algorithm allows one to “switch on” and “off”
 918 this energy term. Figure 11 shows results of micromag-

919 netic simulations for $|\widetilde{M}_y|^2$ and for both CT ’s obtained
 920 with and without dipolar interaction. When the dipolar
 921 interaction is ignored in the micromagnetic computa-
 922 tions, all Fourier coefficients are isotropic at all q and
 923 H investigated (data for $|\widetilde{M}_x|^2$ and $|\widetilde{M}_z|^2$ are not shown).
 924 This observation shows that for any realistic description
 925 of experimental magnetic SANS data this interaction
 926 has to be taken into account.

927 Generally, the sources of the magnetodipolar field
 928 are nonzero divergences of the magnetization ($\nabla \cdot \mathbf{M} \neq$
 929 0). For magnetic nanocomposites, the most prominent

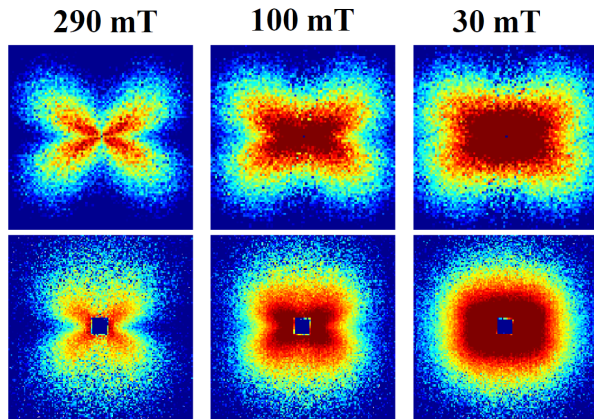


Figure 8: Comparison between simulation (upper row) and experimental data (lower row) for the difference cross section $\propto (|\bar{M}_x|^2 + |\bar{M}_y|^2) \cos^2 \theta + CT \sin \theta \cos \theta$ at different external fields as indicated ($\mathbf{k}_0 \perp \mathbf{H}$). Pixels in the corners of the images have $q \cong 0.64 \text{ nm}^{-1}$. Logarithmic color scale is used. Since the experimental data was not obtained in absolute units, we have multiplied it with a scaling factor for comparison with the simulated data. \mathbf{H} is horizontal in the plane. Experimental data were taken from Ref. [17].

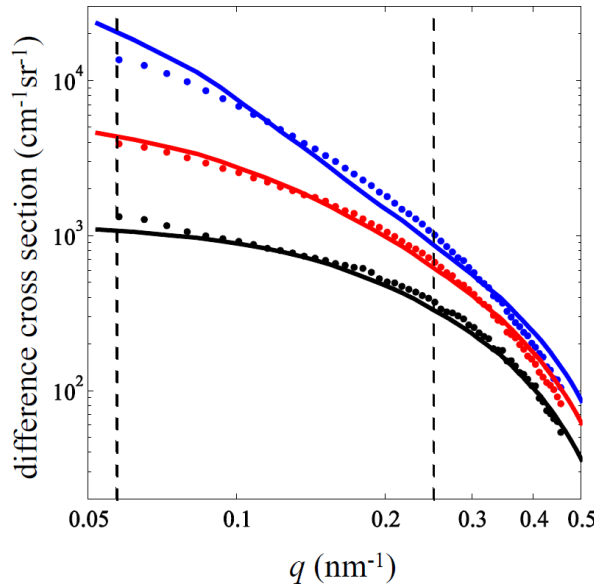


Figure 9: (●) Radially-averaged experimental difference cross sections as a function of momentum transfer q and H ($\mathbf{k}_0 \perp \mathbf{H}$). Field values (in mT) from top to bottom: 30, 100, 290. Solid lines: Results of the micromagnetic simulations (data have been smoothed). Vertical dashed lines indicate the region where the clover-leaf anisotropy is observed. Experimental data were taken from Ref. [17] and multiplied by a scaling factor (compare Fig. 8).

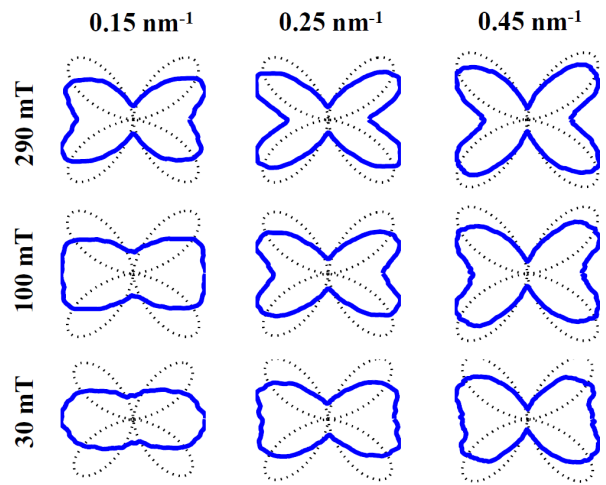


Figure 10: Polar plots of the simulated difference cross section $\propto (|\bar{M}_x|^2 + |\bar{M}_y|^2) \cos^2 \theta + CT \sin \theta \cos \theta$ at different combinations of momentum transfer q and applied magnetic field H (see insets) ($\mathbf{k}_0 \perp \mathbf{H}$). Data have been smoothed. Dotted lines ($\propto \sin^2 \theta \cos^2 \theta$) serve as guides to the eyes.

934 interaction. Such jumps in the magnetic materials pa-
 935 rameters give rise to an inhomogeneous magnetodipolar
 936 field which decorates each nanoparticle and which
 937 causes nanoscale spin deviations within the matrix in
 938 the vicinity of each nanoparticle. Figure 12 displays
 939 the real-space magnetization distribution around two
 940 nanoparticles. Note that the symmetry of the spin struc-
 941 ture replicates the symmetry of the CT (compare to
 942 Fig. 6). In the presence of an applied magnetic field the
 943 stray-field and associated magnetization configuration
 944 around each nanoparticle “look” similar (on the aver-
 945 age), thus giving rise to *dipolar correlations* which add
 946 up to a positive-definite CT contribution to $d\Sigma_M/d\Omega$.
 947 Note, however, that for polycrystalline microstructures
 948 clover-leaf-type anisotropies may become only visible
 949 in $d\Sigma_M/d\Omega$ for $\mathbf{k}_0 \perp \mathbf{H}$.

950 As mentioned above, not only variations in the mag-
 951 netization magnitude, but also variations in the *direc-*
 952 *tion* and/or *magnitude* of magnetic anisotropy \mathbf{K} (ran-
 953 dom anisotropy) and variations in the magnitude of the
 954 exchange coupling may give rise to dipolar correla-
 955 tions. The micromagnetic simulation package allows
 956 us to vary the magnetic materials parameters of both
 957 phases of the nanocomposite. Hence, it becomes pos-
 958 sible to study the impact of such situations on the mag-
 959 netic SANS.

960 In order to investigate variations in \mathbf{K} (which are,
 961 by construction, naturally included into our micromag-
 962 netic algorithm), we have computed the spin distribu-
 963 tion for the situation that $M_h = M_s = M$ (i.e., $\Delta M = 0$)

930 “magnetic volume charges” are related to the nanoscale
 931 variations in the magnetic materials parameters at the
 932 phase boundary between particles and matrix, e.g., vari-
 933 ations in the magnetization, anisotropy or exchange in-

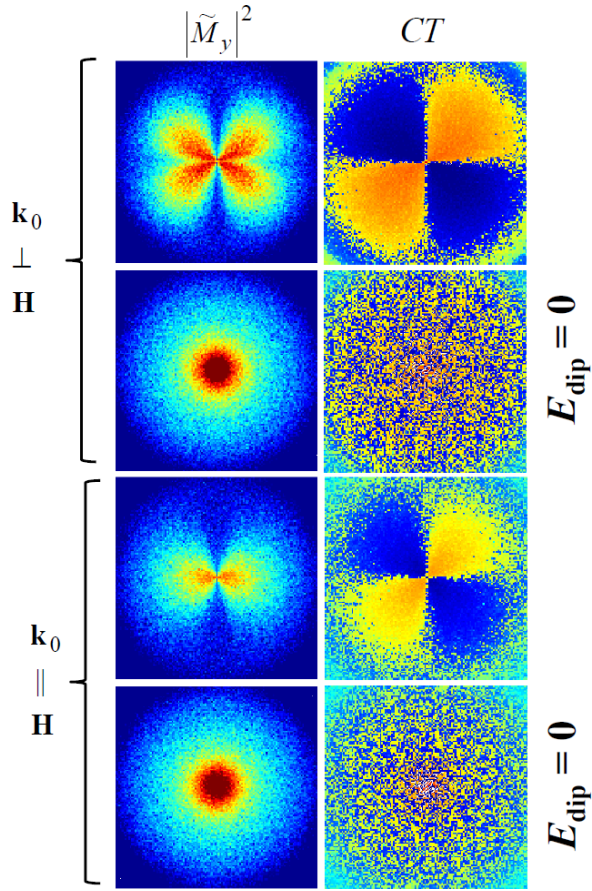


Figure 11: Influence of the dipolar interaction on the Fourier coefficients of the magnetization. $|\tilde{M}_y|^2$ and both cross terms $CT = -(\tilde{M}_y\tilde{M}_z^* + \tilde{M}_y^*\tilde{M}_z)$ ($\mathbf{k}_0 \perp \mathbf{H}$) and $CT = -(\tilde{M}_x\tilde{M}_y^* + \tilde{M}_x^*\tilde{M}_y)$ ($\mathbf{k}_0 \parallel \mathbf{H}$) were computed from a real-space magnetic microstructure with a normalized magnetization of 99.0%. Applied fields of 290 mT (with dipolar interaction) and 7 mT (without dipolar interaction $E_{\text{dip}} = 0$) were required in order to achieve this magnetization value. The corresponding results for the Fourier coefficient $|\tilde{M}_x|^2$ (for $\mathbf{k}_0 \parallel \mathbf{H}$) are analogous to the depicted results for $|\tilde{M}_y|^2$. Pixels in the corners of the images have $q \cong 0.9 \text{ nm}^{-1}$. Logarithmic color scale is used.

964 but for different values of M . Figure 13 reveals that a
 965 clover-leaf-type pattern in $|\tilde{M}_y|^2$ develops with increas-
 966 ing magnetization value M , i.e., with increasing strength
 967 of the magnetodipolar interaction. As jumps in M at
 968 phase boundaries are excluded here as possible sources
 969 for perturbations in the spin structure, it is straightfor-
 970 ward to conclude that nanoscale fluctuations in \mathbf{K} give
 971 rise to inhomogeneous magnetization states, which dec-
 972 orate each nanoparticle and which look similar to the
 973 structure shown in Fig. 12. This observation strongly
 974 suggests that the origin of the clover-leaf pattern in
 975 $d\Sigma_M/d\Omega$ of nanomagnets is not only related to varia-
 976 tions in magnetization magnitude but also due to vari-

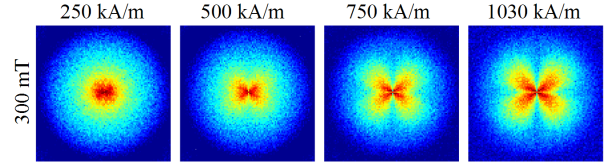


Figure 13: Fourier coefficient $|\tilde{M}_y|^2$ at $\mu_0 H = 0.1 \text{ T}$ and for $M_h = M_s = M$ (i.e., $\Delta M = 0$) ($\mathbf{k}_0 \perp \mathbf{H}$). M increases from left to right (see insets). (upper row) $K_h = 4.6 \times 10^4 \text{ J/m}^3$, $K_s = 1.0 \times 10^2 \text{ J/m}^3$ and random variations in easy-axis directions from particle to particle. (lower row) $K_h = K_s = K_h$ (i.e., $\Delta M = 0$ and $\Delta K = 0$) and random variations in easy-axis directions from particle to particle. Data taken from Ref. [85].

977 ations in the magnitude and direction of the magnetic
 978 anisotropy field.

979 5. Summary and conclusions

980 By means of a recently developed micromagnetic
 981 simulation methodology—especially suited for mod-
 982 eling multi-phase materials—we have computed the
 983 magnetic small-angle neutron scattering (SANS) cross
 984 section $d\Sigma_M/d\Omega$ of a two-phase nanocomposite mag-
 985 net from the NANOPERM family of alloys. Besides
 986 taking into account the full nonlinearity of Brown's
 987 equations of micromagnetics, the approach allows one
 988 to study the dependency of the *individual* magnetiza-
 989 tion Fourier coefficients $\tilde{M}_{(x,y,z)}$ on the applied mag-
 990 netic field \mathbf{H} and, most importantly, on the momentum-
 991 transfer vector \mathbf{q} . This ideally complements neutron
 992 experiments, in which a weighted sum of the $\tilde{M}_{(x,y,z)}$
 993 is generally measured. It is this particular circum-
 994 stance, in conjunction with the flexibility of our mi-
 995 cromagnetic package in terms of microstructure varia-
 996 tion (particle size and distribution, materials param-
 997 eters, texture, etc.), which makes us believe that the ap-
 998 proach of combining full-scale three-dimensional mi-
 999 cromagnetic simulations with experimental magnetic-
 1000 field-dependent SANS data will provide fundamental
 1001 insights into the magnetic SANS of a wide range of
 1002 magnetic materials. The micromagnetic simulations un-
 1003 derline the importance of the magnetodipolar interac-
 1004 tion for understanding magnetic SANS. In particular,
 1005 the so-called clover-leaf-shaped angular anisotropy in
 1006 $d\Sigma_M/d\Omega$ —which was previously believed to be exclu-
 1007 sively related to nanoscale jumps in the magnetization
 1008 magnitude at internal interphases—is of relevance for
 1009 all bulk nanomagnets with spatially fluctuating mag-
 1010 netic parameters.

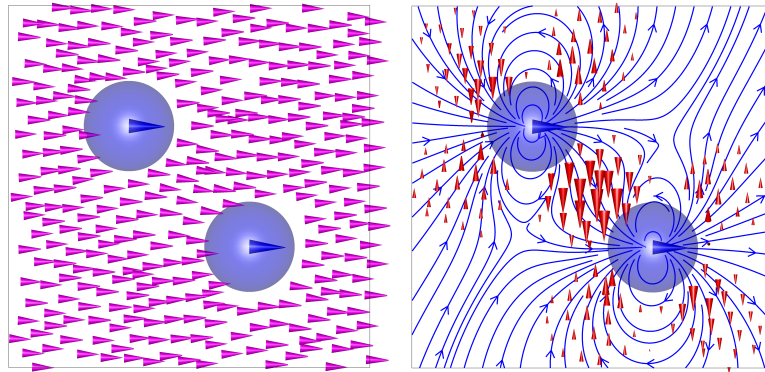


Figure 12: Results of a micromagnetic simulation for the spin distribution around two selected nanoparticles (violet circles), which are assumed to be in a single-domain state. The external magnetic field \mathbf{H} is applied horizontally in the plane ($\mu_0 H = 0.3$ T). Left image: Magnetization distribution in both phases. In order to highlight the spin misalignment in the soft phase, the right image displays the magnetization component \mathbf{M}_\perp perpendicular to \mathbf{H} (red arrows). Thickness of arrows is proportional to the magnitude of \mathbf{M}_\perp . Blue lines: Dipolar field distribution.

Acknowledgments

We thank the Deutsche Forschungsgemeinschaft (Project No. BE 2464/10-1) and the National Research Fund of Luxembourg (ATTRACT Project No. FNR/A09/01 and Project No. FNR/10/AM2c/39) for financial support. Critical reading of the manuscript by Jens-Peter Bick and Dirk Honecker is gratefully acknowledged.

References

- [1] A. Guinier, G. Fournet, *Small-Angle Scattering of X-rays*, Wiley, New York, 1955.
- [2] O. Glatter, O. Kratky (editors), *Small-Angle X-ray Scattering*, Academic Press, London, 1982.
- [3] L. A. Feigin, D. I. Svergun, *Structure Analysis by Small-Angle X-Ray and Neutron Scattering*, Plenum Press, New York, 1987.
- [4] S.-H. Chen, T.-L. Lin, in: D. L. Price, K. Sköld (Eds.), *Methods of Experimental Physics—Neutron Scattering*, Vol. 23-Part B, Academic Press, San Diego, 1987, pp. 489–543.
- [5] P. Lindner, T. Zemb (editors), *Neutron, X-Ray and Light Scattering: Introduction to an Investigative Tool for Colloidal and Polymeric Systems*, North Holland, Amsterdam, 1991.
- [6] J. S. Pedersen, in: P. Lindner, T. Zemb (Eds.), *Neutrons, X-Rays and Light: Scattering Methods Applied to Soft Condensed Matter*, Elsevier, Amsterdam, 2002, pp. 391–420.
- [7] D. I. Svergun, M. H. J. Koch, *Rep. Prog. Phys.* 66 (2003) 1735.
- [8] H. B. Stuhmann, *Rep. Prog. Phys.* 67 (2004) 1073.
- [9] Y. B. Melnichenko, G. D. Wignall, *J. Appl. Phys.* 102 (2007) 021101.
- [10] A. Heinemann, H. Hermann, A. Wiedenmann, N. Mattern, K. Wetzig, *J. Appl. Cryst.* 33 (2000) 1386.
- [11] H. Hermann, A. Heinemann, N. Mattern, A. Wiedenmann, *Europhys. Lett.* 51 (2000) 127.
- [12] A. Michels, R. N. Viswanath, J. Weissmüller, *Europhys. Lett.* 64 (2003) 43.
- [13] A. Grob, S. Saranu, U. Herr, A. Michels, R. N. Viswanath, J. Weissmüller, *Phys. Status Solidi A* 201 (2004) 3354.
- [14] W. Wagner, J. Kohlbrecher, in: Y. Zhu (Ed.), *Modern Techniques for Characterizing Magnetic Materials*, Kluwer Academic Publishers, Boston, 2005, pp. 65–103.
- [15] A. Michels, C. Vecchini, O. Moze, K. Suzuki, J. M. Cadogan, P. K. Pranzas, J. Weissmüller, *Europhys. Lett.* 72 (2005) 249.
- [16] C. Vecchini, O. Moze, K. Suzuki, P. K. Pranzas, J. Weissmüller, A. Michels, *Appl. Phys. Lett.* 87 (2005) 202509.
- [17] A. Michels, C. Vecchini, O. Moze, K. Suzuki, P. K. Pranzas, J. Kohlbrecher, J. Weissmüller, *Phys. Rev. B* 74 (2006) 134407.
- [18] D. Honecker, A. Ferdinand, F. Döbrich, C. D. Dewhurst, A. Wiedenmann, C. Gómez-Polo, K. Suzuki, A. Michels, *Eur. Phys. J. B* 76 (2010) 209–213.
- [19] A. Michels, D. Honecker, F. Döbrich, C. D. Dewhurst, K. Suzuki, A. Heinemann, *Phys. Rev. B* 85 (2012) 184417.
- [20] A. Bracchi, K. Samwer, P. Schaaf, J. F. Löffler, S. Schneider, *Mater. Sci. Eng. A* 375–377 (2004) 1027.
- [21] E. García-Matres, A. Wiedenmann, G. Kumar, J. Eckert, H. Hermann, L. Schultz, *Phys. B* 350 (2004) e315.
- [22] R. García Calderón, L. Fernández Barquín, S. N. Kaul, J. C. Gómez Sal, P. Gorria, J. S. Pedersen, R. K. Heenan, *Phys. Rev. B* 71 (2005) 134413.
- [23] K. Mergia, S. Messori, *J. Phys.: Condens. Matter* 20 (2008) 104219.
- [24] A. Michels, J. Weissmüller, A. Wiedenmann, J. G. Barker, *J. Appl. Phys.* 87 (2000) 5953.
- [25] A. Michels, J. Weissmüller, A. Wiedenmann, J. S. Pedersen, J. G. Barker, *Philos. Mag. Lett.* 80 (2000) 785.
- [26] A. Michels, J. Weissmüller, U. Erb, J. G. Barker, *Phys. Status Solidi A* 189 (2002) 509.
- [27] A. Michels, J. Weissmüller, R. Birringer, *Eur. Phys. J. B* 29 (2002) 533.
- [28] A. Michels, R. N. Viswanath, J. G. Barker, R. Birringer, J. Weissmüller, *Phys. Rev. Lett.* 91 (2003) 267204.
- [29] J. Weissmüller, A. Michels, D. Michels, A. Wiedenmann, C. E. Krill III, H. M. Sauer, R. Birringer, *Phys. Rev. B* 69 (2004) 054402.
- [30] J. F. Löffler, H. B. Braun, W. Wagner, G. Kostorz, A. Wiedenmann, *Phys. Rev. B* 71 (2005) 134410.
- [31] A. Michels, J. Weissmüller, *Rep. Prog. Phys.* 71 (2008) 066501.
- [32] A. Michels, F. Döbrich, M. Elmas, A. Ferdinand, J. Markmann, M. Sharp, H. Eckerlebe, J. Kohlbrecher, R. Birringer, *EPL* 81 (2008) 66003.
- [33] A. Michels, M. Elmas, F. Döbrich, M. Ames, J. Markmann,

- 1090 M. Sharp, H. Eckerlebe, J. Kohlbrecher, R. Birringer, *EPL* 85 1155
1091 (2009) 47003. 1156
- 1092 [34] D. Honecker, F. Döbrich, C. D. Dewhurst, A. Wiedenmann, 1157
1093 A. Michels, *J. Phys.: Condens. Matter* 23 (2011) 016003. 1158
- 1094 [35] F. Döbrich, J. Kohlbrecher, M. Sharp, H. Eckerlebe, R. Bir- 1159
1095 ringer, A. Michels, *Phys. Rev. B* 85 (2012) 094411. 1160
- 1096 [36] B. van den Brandt, H. Glättli, I. Grillo, P. Hautle, H. Jouve, 1161
1097 J. Kohlbrecher, J. A. Konter, E. Leymarie, S. Mango, R. P. May, 1162
1098 A. Michels, H. B. Stuhmann, O. Zimmer, *Eur. Phys. J. B* 49 1163
1099 (2006) 157. 1164
- 1100 [37] M. Laver, E. M. Forgan, S. P. Brown, D. Charalambous, 1165
1101 D. Fort, C. Bowell, S. Ramos, R. J. Lycett, D. K. Christen, 1166
1102 J. Kohlbrecher, C. D. Dewhurst, R. Cubitt, *Phys. Rev. Lett.* 96 1167
1103 (2006) 167002. 1168
- 1104 [38] M. R. Eskildsen, E. M. Forgan, H. Kawano-Furukawa, *Rep.* 1169
1105 *Prog. Phys.* 74 (2011) 124504. 1170
- 1106 [39] M. Bischof, P. Staron, A. Michels, P. Granitzer, K. Rumpf, 1171
1107 H. Leitner, C. Scheu, H. Clemens, *Acta mater.* 55 (2007) 2637. 1172
- 1108 [40] G. Balaji, S. Ghosh, F. Döbrich, H. Eckerlebe, J. Weissmüller, 1173
1109 *Phys. Rev. Lett.* 100 (2008) 227202. 1174
- 1110 [41] A. Kreyssig, R. Prozorov, C. D. Dewhurst, P. C. Canfield, R. W. 1175
1111 McCallum, A. I. Goldman, *Phys. Rev. Lett.* 102 (2009) 047204. 1176
- 1112 [42] F. Gazeau, E. Dubois, J.-C. Bacri, F. Boué, A. Cebers, 1177
1113 R. Perzynski, *Phys. Rev. E* 65 (2002) 031403. 1178
- 1114 [43] T. Thomson, S. L. Lee, M. F. Toney, C. D. Dewhurst, F. Y. Ogrin, 1179
1115 C. J. Oates, S. Sun, *Phys. Rev. B* 72 (2005) 064441. 1180
- 1116 [44] Y. Ijiri, C. V. Kelly, J. A. Borchers, J. J. Rhyne, D. F. Farrell, 1181
1117 S. A. Majetich, *Appl. Phys. Lett.* 86 (2005) 243102. 1182
- 1118 [45] A. Wiedenmann, U. Keiderling, K. Habicht, M. Russina, 1183
1119 R. Gähler, *Phys. Rev. Lett.* 97 (2006) 057202. 1184
- 1120 [46] N. A. Grigoryeva, S. V. Grigoriev, H. Eckerlebe, A. A. Eliseev, 1185
1121 A. V. Lukashin, K. S. Napolskii, *J. Appl. Cryst.* 40 (2007) s532. 1186
- 1122 [47] K. S. Napolskii, A. A. Eliseev, N. V. Yesin, A. V. Lukashin, 1187
1123 Y. D. Tretyakov, N. A. Grigorieva, S. V. Grigoriev, H. Eckerlebe, 1188
1124 *Physica E* 37 (2007) 178. 1189
- 1125 [48] M. Bonini, A. Wiedenmann, P. Baglioni, *J. Appl. Cryst.* 40 1190
1126 (2007) s254. 1191
- 1127 [49] T. Oku, T. Kikuchi, T. Shinohara, J. Suzuki, Y. Ishii, M. Takeda, 1192
1128 K. Kakurai, Y. Sasaki, M. Kishimoto, M. Yokoyama, Y. Nishi- 1193
1129 hara, *Physica B* 404 (2009) 2575. 1194
- 1130 [50] S. V. Grigoriev, A. V. Syromyatnikov, A. P. Chumakov, N. A. 1195
1131 Grigoryeva, K. S. Napolskii, I. V. Roslyakov, A. A. Eliseev, 1196
1132 A. V. Petukhov, H. Eckerlebe, *Phys. Rev. B* 81 (2010) 125405. 1197
- 1133 [51] K. L. Krycka, R. A. Booth, C. R. Hogg, Y. Ijiri, J. A. Borchers, 1198
1134 W. C. Chen, S. M. Watson, M. Laver, T. R. Gentile, L. R. De- 1199
1135 don, S. Harris, J. J. Rhyne, S. A. Majetich, *Phys. Rev. Lett.* 104 1200
1136 (2010) 207203. 1201
- 1137 [52] S. Disch, E. Wetterskog, R. P. Hermann, A. Wiedenmann, 1202
1138 U. Vainio, G. Salazar-Alvarez, L. Bergström, T. Brückel, *New* 1203
1139 *J. Phys.* 14 (2012) 013025. 1204
- 1140 [53] M. Laver, C. Mudivarthi, J. R. Cullen, A. B. Flatau, W.-C. Chen, 1205
1141 S. M. Watson, M. Wuttig, *Phys. Rev. Lett.* 105 (2010) 027202. 1206
- 1142 [54] B. G. Ueland, J. W. Lynn, M. Laver, Y. J. Choi, S.-W. Cheong, 1207
1143 *Phys. Rev. Lett.* 104 (2010) 147204. 1208
- 1144 [55] S. J. Lister, T. Thomson, J. Kohlbrecher, K. Takano, 1209
1145 V. Venkataramana, S. J. Ray, M. P. Wismayer, M. A. de Vries, 1210
1146 H. Do, Y. Ikeda, S. L. Lee, *Appl. Phys. Lett.* 97 (2010) 112503. 1211
- 1147 [56] C. Dufour, M. R. Fitzsimmons, J. A. Borchers, M. Laver, K. L. 1212
1148 Krycka, K. Dumesnil, S. M. Watson, W. C. Chen, J. Won, 1213
1149 S. Singh, *Phys. Rev. B* 84 (2011) 064420. 1214
- 1150 [57] C. Pappas, E. Lelièvre-Berna, P. Falus, P. M. Bentley, 1215
1151 E. Moskvina, S. Grigoriev, P. Fouquet, B. Farago, *Phys. Rev. Lett.* 1216
1152 102 (2009) 197202. 1217
- 1153 [58] S. V. Grigoriev, D. Chernyshov, V. A. Dyadkin, V. Dmitriev, 1218
1154 S. V. Maleyev, E. V. Moskvina, D. Menzel, J. Schoenes, H. Eck- 1219
erlebe, *Phys. Rev. Lett.* 102 (2009) 037204. 1220
- [59] S. Mühlbauer, B. Binz, F. Jonietz, C. Pfleiderer, A. Rosch, 1221
A. Neubauer, R. Georgii, P. Böni, *Science* 323 (2009) 915. 1222
- [60] W. F. Brown Jr., *Micromagnetics*, Interscience Publishers, New 1223
York, 1963. 1224
- [61] A. Aharoni, *Introduction to the Theory of Ferromagnetism*, 2nd 1225
Edition, Clarendon Press, Oxford, 1996. 1226
- [62] H. Kronmüller, M. Fähnle, *Micromagnetism and the Mi- 1227
crostructure of Ferromagnetic Solids*, Cambridge University 1228
Press, Cambridge, 2003. 1229
- [63] H. Kronmüller, A. Seeger, M. Wilkens, *Z. Phys.* 171 (1963) 291. 1230
- [64] K. Suzuki, G. Herzer, in: D. Sellmyer, R. Skomski (Eds.), *Ad- 1231
vanced Magnetic Nanostructures*, Springer, New York, 2006, 1232
pp. 365–401. 1233
- [65] H. Kronmüller, S. Parkin, *Handbook of Magnetism and Ad- 1234
vanced Magnetic Materials*, John Wiley & Sons, Chichester, 1235
2007, vol.2, pp.795. 1236
- [66] J. Fidler, P. Speckmayer, T. Schrefl, D. Suess, *J. Appl. Phys.* 97 1237
(2005) 10E508. 1238
- [67] F. Y. Ogrin, S. L. Lee, M. Wismayer, T. Thomson, C. D. De- 1239
wurst, R. Cubitt, S. M. Weekes, *J. Appl. Phys.* 99 (2006) 1240
08G912. 1241
- [68] S. Saranu, A. Grob, J. Weissmüller, U. Herr, *Phys. Status Solidi* 1242
A 205 (2008) 1774. 1243
- [69] M. Donahue, D. Porter, *The Object Oriented MicroMagnetic* 1244
Framework (OOMMF). 1245
URL <http://math.nist.gov/oommf/> 1246
- [70] W. S. Jodrey, E. M. Tory, *Phys. Rev. A* 32 (1985) 2347. 1247
- [71] O. Gutfleisch, K.-H. Müller, K. Khlopkov, M. Wolf, A. Yan, 1248
R. Schäfer, T. Gemming, L. Schultz, *Acta Mater.* 54 (2006) 997. 1249
- [72] G. Hrkac, T. G. Woodcock, C. Freeman, A. Goncharov, J. Dean, 1250
T. Schrefl, O. Gutfleisch, *Appl. Phys. Lett.* 97 (2010) 232511. 1251
- [73] D. V. Berkov, N. L. Gorn, in *Handbook of Advanced Magne- 1252
tic Materials*, Vol. 2, Springer Verlag and Tsinghua University 1253
Press, 2005, pp. 421–507, edited by Y. Liu, D. Shindo and D. J. 1254
Sellmyer. 1255
- [74] S. Erokhin, D. Berkov, N. Gorn, A. Michels, *IEEE Trans. Magn.* 1256
47 (2011) 3044. 1257
- [75] P. Gibbon, G. Sutmann, in *Quantum Simulations of Complex* 1258
Many-Body Systems: From Theory to Algorithms, Lecture 1259
Notes, edited by J. Grotendorst, D. Marx and A. Muramatsu 10 1260
(2002) 467–506. 1261
- [76] D. V. Berkov, N. L. Gorn, *Phys. Rev. B* 57 (1998) 14332. 1262
- [77] N. L. Gorn, D. V. Berkov, P. Gönert, D. Stock, *J. Magn. Magn.* 1263
Mat. 310 (2007) 2829. 1264
- [78] R. W. Hockney, J. W. Eastwood, *Computer simulation using par- 1265
ticles*, McGraw-Hill, 1981. 1266
- [79] M. Deserno, C. Holm, *J. Chem. Phys.* 109 (1998) 7678. 1267
- [80] L. Landau, E. Lifshitz, *Phys. Z. Sowjetunion* 8 (1935) 153. 1268
- [81] D. V. Berkov, N. L. Gorn, *Micromagus: package for micromag- 1269
netic simulations*. 1270
URL <http://www.micromagus.de> 1271
- [82] S. Erokhin, D. Berkov, N. Gorn, A. Michels, *Phys. Rev. B* 85 1272
(2012) 024410. 1273
- [83] W. Rave, K. Fabian, A. Hubert, *J. Magn. Magn. Mater.* 190 1274
(1998) 332. 1275
- [84] A. Wiedenmann, *Collection SFN* 11 (2010) 219, 1276
<http://www.neutron-sciences.org/>. 1277
- [85] S. Erokhin, D. Berkov, N. Gorn, A. Michels, *Phys. Rev. B* 85 1278
(2012) 134418. 1279